Modeling of elasto-capillary phenomena†

David L. Henann*[a] and Katia Bertoldi*[bc]

Surface energy is an important factor in the deformation of fluids but is typically a minimal or negligible effect in solids. However, when a solid is soft and its characteristic dimension is small, forces due to surface energy can become important and induce significant elastic deformation. The interplay between surface energy and elasticity can lead to interesting elasto-capillary phenomena. We present a finite-element-based numerical simulation capability for modeling these effects in a static, implicit framework. We demonstrate the capacity of the simulation capability by examining three elasto-capillary problems: (i) wetting of an elastic hemispherical droplet on a substrate, (ii) cavitation of an elastomer, and (iii) the Rayleigh–Plateau instability in soft elastic filaments.

1 Introduction

A common concept in the study of fluid mechanics is that of surface tension, which arises due to a constant free energy density associated with the surface. For an incompressible, Newtonian fluid, changes in the surface energy are the only contribution to changes in the free energy, driving a fluid body to minimize its surface area in an effort to minimize free energy.[1] However, if the body is elastic, the accumulation of elastic strain through deformation also contributes to the free energy. Typically for solids, volumetric elastic strain energy dominates, but in certain cases, the surface and elastic energy scales are comparable, leading to an interesting interplay.[2–22]

To make this idea more concrete, consider a soft material with shear modulus G, surface energy density γ, volume V, and surface area A. Surface energy will scale as γA, while volumetric strain energy scales as GV. Defining a characteristic length $\ell = V/A$, the ratio of surface energy to strain energy is $\gamma/G\ell$, which we refer to as the *elasto-capillary number*. As $\gamma/G\ell \to \infty$, surface energy is the main contributor to the free energy, and fluid behavior dominates. Conversely, when $\gamma/G\ell \approx 0$, elastic effects dominate, and we recover the familiar case of elastic solids. For example, for a rubber with shear modulus of 1 MPa, surface energy of 1 J m^{-2}, and a characteristic length of 1 mm, the elasto-capillary number is 0.001, and surface tension will be a negligible effect. However, for a soft gel with shear modulus of 1 kPa, surface energy of 0.1 J m^{-2}, and characteristic dimension of 100 μm, the elasto-capillary number is unity, and elasto-capillary coupling will be observed.

Specific examples of elasto-capillary phenomena are quite diverse. Surface tension forces can serve to flatten rough surfaces on an elastic substrate[4] or cause deformation of a soft elastic body at a contact line.[5–10] A number of instabilities in soft solids are either caused or affected by the presence of surface tension. The Rayleigh–Plateau instability, in which surface tension leads to the break-up of a fluid jet, also occurs in thin elastic filaments;[11] however, break-up of the filament is prevented due to the elasticity of the material, leaving a stable undulatory shape. Additionally, surface tension serves as a barrier for familiar instabilities in soft materials, such as creasing,[12–14] wrinkling,[15] and cavitation.[16–22]

It is important to make clear when the assumption of constant surface energy density, and hence the idea of surface tension, is applicable to a solid. For a fluid surface, the energetics are quite simple – the free energy density of a surface is constant. Mechanically, atoms or molecules in a fluid are capable of moving back and forth from the bulk to the surface, allowing the fluid to change its surface area without stretching bonds between particles. This constant surface energy density leads to a constant isotropic surface stress – the surface tension. Conversely, for many solid surfaces, such as those comprised of a crystallographic plane in a crystalline material, atoms or molecules have significantly less mobility, particularly at low homologous temperatures. Consequently, changes in surface area are predominately accommodated through the stretching of bonds between particles on the surface, leading to a non-constant and non-isotropic surface stress. In this work, we focus attention upon soft, amorphous polymeric materials that are lightly cross-linked. In this case, molecules have sufficient mobility to move from the bulk to the surface and *vice versa*, and thus, the behavior of surfaces of these soft materials is indeed fluid-like.

[a]*School of Engineering, Brown University, Providence, RI, USA. E-mail: david_henann@brown.edu*

[b]*School of Engineering and Applied Sciences, Harvard University, Cambridge, MA, USA. E-mail: bertoldi@seas.harvard.edu*

[c]*Kavli Institute for Bionano Science and Technology, Harvard University, Cambridge, MA, USA*

Modeling of elasto-capillary phenomena requires (i) mathematically describing both the behavior of the surface and the bulk and (ii) numerical methods for solving the resulting system of equations in arbitrary settings. Continuum modeling of surfaces is a robust field, going back to the seminal work of Gurtin and Murdoch[23] and expanded upon over the decades for a variety of different problems.[24–28] However, a need remains for numerical procedures appropriate for modeling elasto-capillary phenomena. Specifically, a variational formulation and finite-element implementation of the elasto-capillary problem, which may be paired with standard techniques for modeling rubbery materials is lacking. Several in-house finite-element codes for fluids[29] and solids[30–32] exist, but these are not available to the wider research community. The purpose of this paper to develop a finite-element implementation of the elasto-capillary problem in the commercial finite-element code Abaqus/Standard[33] and to use the code to study a variety of elasto-capillary problems.

In Section 2, we mathematically describe the elasto-capillary problem, highlighting the variational form. In Section 3, we lay out the finite-element formulation, and in Section 4, we address three different elasto-capillary problems: (i) wetting of an elastic droplet, (ii) cavitation of an elastomer, and (iii) the Rayleigh–Plateau instability in thin elastic filaments. Through these varied applications, we demonstrate the robustness of the capability as well as provide new insights into these problems.

2 Continuum framework

2.1 Kinematics

We consider a homogeneous body B identified with the region of space it occupies in a fixed reference configuration and denote by $\mathbf{X}$ an arbitrary material point of B, as shown in Fig. 1. A motion of B is then a smooth one-to-one mapping $\mathbf{x} = \boldsymbol{\chi}(\mathbf{X}, t)$ with deformation gradient given by‡

$$\mathbf{F} = \nabla\boldsymbol{\chi}, \tag{1}$$

such that $J = \det\mathbf{F} > 0$. The right and left and polar decompositions of $\mathbf{F}$ are given by $\mathbf{F} = \mathbf{R}\mathbf{U} = \mathbf{V}\mathbf{R}$, where $\mathbf{R}$ is a rotation (proper orthogonal tensor), while $\mathbf{U}$ and $\mathbf{V}$ are symmetric, positive-definite stretch tensors. Also, the right and left Cauchy–Green tensors are given by $\mathbf{C} = \mathbf{U}^2 = \mathbf{F}^\top\mathbf{F}$ and $\mathbf{B} = \mathbf{V}^2 = \mathbf{F}\mathbf{F}^\top$, respectively.

2.2 Equilibrium

With reference to Fig. 1, the region of space occupied by the body at time t is denoted by $\mathscr{B}$ and referred to as the deformed body. Neglecting inertial effects, the balance of forces and moments in $\mathscr{B}$ are expressed in the deformed body as

$$\mathrm{div}\mathbf{T} + \mathbf{b}_0 = \mathbf{0} \quad \text{and} \quad \mathbf{T} = \mathbf{T}^\top, \tag{2}$$

‡ The symbols ∇ and Div denote the gradient and divergence with respect to the material point $\mathbf{X}$ in the reference configuration; grad and div denote these operators with respect to the point $\mathbf{x} = \boldsymbol{\chi}(\mathbf{X}, t)$ in the deformed configuration. We write tr$\mathbf{A}$, det$\mathbf{A}$, and dev$\mathbf{A}$ to denote the trace, determinant, and deviatoric part of a tensor $\mathbf{A}$, respectively.
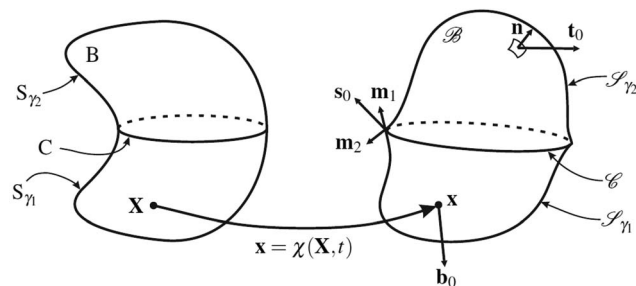

Fig. 1 The reference body B and the deformed body $\mathscr{B}$ at time t.

respectively, where $\mathbf{T}$ is the Cauchy stress and $\mathbf{b}_0$ is an external body force per unit deformed volume.

The boundary of the deformed body, $\mathscr{S} = \partial\mathscr{B}$, has outward unit normal $\mathbf{n}$. For illustrative purposes, we consider two complementary subsurfaces $\mathscr{S}_{\gamma_1}$ and $\mathscr{S}_{\gamma_2}$ ($\mathscr{S} = \mathscr{S}_{\gamma_1} \cup \mathscr{S}_{\gamma_2}$) and denote the closed curve, which forms the boundary of these subsurfaces, as $\mathscr{C} = \partial\mathscr{S}_{\gamma_1} = \partial\mathscr{S}_{\gamma_2}$ (see Fig. 1). We introduce the unit vector $\mathbf{m}_1$, which is normal to $\mathscr{C}$, tangent to $\mathscr{S}_{\gamma_1}$, and oriented outward from this surface. The unit vector $\mathbf{m}_2$ is defined analogously for $\mathscr{S}_{\gamma_2}$. We allow the surface tension to vary smoothly on each subsurface and to undergo a discontinuity across the curve $\mathscr{C}$. Moreover, we do not require smoothness of $\mathscr{S}$ across the curve $\mathscr{C}$. Allowing for a discontinuity in the surface tension and non-smoothness of $\mathscr{S}$ across $\mathscr{C}$ opens the door to the modeling of contact lines.

The balance of forces on each subsurface $\mathscr{S}_{\gamma_n}$ is then given by§

$$2H\gamma_n\mathbf{n} + \mathrm{grad}_{\mathscr{S}}\gamma_n + \mathbf{t}_0 = \mathbf{T}\mathbf{n}, \tag{3}$$

where $H = -(1/2)\mathrm{div}_{\mathscr{S}}\mathbf{n}$ is the mean curvature of the surface, γ_n is the smoothly-varying surface tension on the subsurface $\mathscr{S}_{\gamma_n}$, and $\mathbf{t}_0$ is an external traction per unit deformed area. The first term, which accounts for surface curvature, is the commonly-encounted term from the Young–Laplace equation, and the second term accounts for surface tension gradients, commonly referred to as Marangoni effects in the context of fluid mechanics.

Finally, the balance of forces on the curve $\mathscr{C}$ is

$$\mathbf{s}_0 = \gamma_1\mathbf{m}_1 + \gamma_2\mathbf{m}_2, \tag{4}$$

where $\mathbf{s}_0$ is an external line force per unit deformed length.

In order to recast the equations of equilibrium in a variational formulation, we introduce a vector test field $\mathbf{w}$ and write (2)–(4) in the weak form

$$\int_{\mathscr{B}}(-\mathbf{T}:\mathrm{grad}\mathbf{w} + \mathbf{b}_0\cdot\mathbf{w})\mathrm{d}v + \sum_n\int_{\mathscr{S}_{\gamma_n}}(2H\gamma_n\mathbf{n} + \mathrm{grad}_{\mathscr{S}}\gamma_n + \mathbf{t}_0)\cdot\mathbf{w}\mathrm{d}a$$
$$+ \int_{\mathscr{C}}(-\gamma_1\mathbf{m}_1 - \gamma_2\mathbf{m}_2 + \mathbf{s}_0)\cdot\mathbf{w}\mathrm{d}s = 0, \tag{5}$$

§ We introduce the surface differential operators $\mathrm{grad}_{\mathscr{S}}$ and $\mathrm{div}_{\mathscr{S}}$ to denote the surface gradient and surface divergence, respectively, in the deformed configuration.[23,28]

where we have invoked the divergence theorem as is standard. In order to manipulate the surface terms, we note

$$\int_{\mathscr{S}_{\gamma_n}} \mathrm{div}_{\mathscr{S}}(\gamma_n \mathbf{w}) \mathrm{d}a = \int_{\mathscr{S}_{\gamma_n}} (\mathrm{grad}_{\mathscr{S}} \gamma_n \cdot \mathbf{w} + \gamma_n \mathrm{div}_{\mathscr{S}} \mathbf{w}) \mathrm{d}a$$
$$= \int_{\mathscr{C}} \gamma_n \mathbf{w} \cdot \mathbf{m}_n \mathrm{d}s - \int_{\mathscr{S}_{\gamma_n}} 2H \gamma_n \mathbf{w} \cdot \mathbf{n} \mathrm{d}a. \quad (6)$$

The first line is an application of the product rule, while the second line invokes the surface divergence theorem.[23,28] Substituting (6) for $n = 1, 2$ into (5), we have

$$\int_{\mathscr{B}} \mathbf{T} : \mathrm{grad}\mathbf{w}\mathrm{d}v + \int_{\mathscr{S}} \gamma \mathrm{div}_{\mathscr{S}} \mathbf{w} \mathrm{d}a = \int_{\mathscr{B}} \mathbf{b}_0 \cdot \mathbf{w} \mathrm{d}v$$
$$+ \int_{\mathscr{S}} \mathbf{t}_0 \cdot \mathbf{w} \mathrm{d}a + \int_{\mathscr{C}} \mathbf{s}_0 \cdot \mathbf{w} \mathrm{d}s, \quad (7)$$

where we have used the fact that the union of the subsurfaces $\mathscr{S}_{\gamma_n}$ is the total boundary $\mathscr{S}$. This succinct representation of equilibrium encompasses the forces balances (2)–(4), allowing the surface tension γ to vary smoothly over the surface and undergo discontinuities. While the derivation of (7) is based upon dividing $\partial\mathscr{B}$ into two subsurfaces, joined by a closed curve $\mathscr{C}$, it is straightforward to generalize the result to an arbitrary set of complementary subsurfaces and corresponding boundary curves.

Finally, we note that when the test function $\mathbf{w}$ is interpreted as a virtual velocity field, eqn (7) represents a statement of the principle of virtual power, wherein the left side represents the expenditure of internal power while the right side represents the expenditure of external power. This statement of equilibrium may be used as a starting point to derive the strong form of equilibrium (2)–(4) by reversing the arguments of this section.

2.3 Constitutive equations

We consider a hyperelastic material whose constitutive response is described by a referential free energy density function $\psi_R = \hat{\psi}_R(\mathbf{F})$. The laws of thermodynamics then dictate that the Cauchy stress be given by

$$\mathbf{T} = J^{-1} \frac{\mathrm{d}\hat{\psi}_R(\mathbf{F})}{\mathrm{d}\mathbf{F}} \mathbf{F}^{\top}. \quad (8)$$

Frame indifference requires that the free energy function be independent of the frame of reference, which may be achieved by writing the free energy as a function of the right Cauchy–Green tensor $\mathbf{C}$. Moreover, for an isotropic material, the free energy may be expressed as a function of the invariants of $\mathbf{C}$:

$$I_1 = \mathrm{tr}\mathbf{C}, \quad I_2 = \mathrm{tr}(\mathbf{C}^2), \quad I_3 = \mathrm{tr}(\mathbf{C}^3). \quad (9)$$

With the aim of modeling nearly-incompressible materials, we denote the distortional part of $\mathbf{F}$ by

$$\mathbf{F}_{\mathrm{dis}} \overset{\mathrm{def}}{=} J^{-1/3}\mathbf{F}, \quad \mathrm{det}\mathbf{F}_{\mathrm{dis}} = 1 \quad (10)$$

and correspondingly let

$$\mathbf{C}_{\mathrm{dis}} \overset{\mathrm{def}}{=} (\mathbf{F}_{\mathrm{dis}})^{\top}\mathbf{F}_{\mathrm{dis}} = J^{-2/3}\mathbf{C}$$
$$\mathbf{B}_{\mathrm{dis}} \overset{\mathrm{def}}{=} \mathbf{F}_{\mathrm{dis}}(\mathbf{F}_{\mathrm{dis}})^{\top} = J^{-2/3}\mathbf{B} \quad (11)$$

denote the distortional right and left Cauchy–Green tensors, respectively. Defining the invariants

$$\bar{I}_1 = \mathrm{tr}(\mathbf{C}_{\mathrm{dis}}) \text{ and } \bar{I}_2 = \mathrm{tr}(\mathbf{C}_{\mathrm{dis}}^2), \quad (12)$$

we take the free energy function to be given by $\psi_R = \bar{\psi}_R(\bar{I}_1, \bar{I}_2, J)$.

Here, we use a Gent free energy[34]

$$\psi_R = -\frac{1}{2}GI_{\mathrm{m}} \ln\left(1 - \frac{\bar{I}_1 - 3}{I_{\mathrm{m}}}\right) + \frac{1}{2}K(J-1)^2, \quad (13)$$

for which the stress is given by

$$\mathbf{T} = J^{-1}G\left(1 - \frac{\bar{I}_1 - 3}{I_{\mathrm{m}}}\right)^{-1} \mathrm{dev}(\mathbf{B}_{\mathrm{dis}}) + K(J-1)\mathbf{1}, \quad (14)$$

where G and K are the ground-state shear and bulk moduli, respectively. Moreover, I_{m} represents the upper limit of $(\bar{I}_1 - 3)$ associated with limited chain extensibility of polymeric molecules. Throughout, in order to model nearly incompressible materials, we take $K/G = 1000$.

Note that as $I_{\mathrm{m}} \to \infty$, (13) reduces to the Neo-Hookean free energy function

$$\psi_R = \frac{1}{2}G(\bar{I}_1 - 3) + \frac{1}{2}K(J-1)^2, \quad (15)$$

so that

$$\mathbf{T} = J^{-1}G\mathrm{dev}(\mathbf{B}_{\mathrm{dis}}) + K(J-1)\mathbf{1}. \quad (16)$$

For the simulations presented in Section 4, we utilize the Neo-Hookean free energy function (15) for situations involving small to moderate stretches, while for larger stretches, we use the Gent free energy (13).

In the applications section of this paper, we consider several instabilities. To ease the process of modeling instabilities, we add time-dependence to the material response. In the rheological sense, we add a finite-deformation Maxwell element in parallel with the hyperelastic behavior described above. This viscoelastic response is not intended to model any real behavior and does not affect the simulation results reported in this paper. For this reason, we relegate a detailed description of the viscoelastic model to Appendix A.

3 Finite-element numerical solution procedure

In this section, we describe our numerical solution procedure using finite elements in Abaqus/Standard.[33] The body is approximated using finite elements, $\mathscr{B} = \cup\mathscr{B}^{\mathrm{e}}$. The nodal solution variable is taken to be the displacement, which is interpolated inside each element by

$$\mathbf{u} = \sum_A \mathbf{u}^A N^A, \quad (17)$$

with the index $A = 1, 2, \ldots$ denoting the nodes of the element, $\mathbf{u}^A$ nodal displacements, and N^A the shape functions. We employ a

standard Galerkin approach in that the test field is interpolated by the same shape functions,

$$\mathbf{w} = \sum_A \mathbf{w}^A N^A. \tag{18}$$

Using (17) and (18) in (7) yields the following element-level system of equations:

$$\int_{\mathcal{B}^e} \mathbf{T} \mathrm{grad} N^A \mathrm{d}v + \int_{\mathcal{S}^e} \gamma \mathrm{grad}_{\mathcal{S}} N^A \mathrm{d}a$$
$$= \int_{\mathcal{B}^e} \mathbf{b}_0 N^A \mathrm{d}v + \int_{\mathcal{S}^e} \mathbf{t}_0 N^A \mathrm{d}a + \int_{\mathcal{C}^e} \mathbf{s}_0 N^A \mathrm{d}s. \tag{19}$$

This system of equations is solved iteratively using a Newton procedure by defining the following element-level residuals

$$\mathbf{R}_{\mathbf{u}}^A = -\int_{\mathcal{B}^e} \mathbf{T} \mathrm{grad} N^A \mathrm{d}v - \int_{\mathcal{S}^e} \gamma \mathrm{grad}_{\mathcal{S}} N^A \mathrm{d}a + \int_{\mathcal{B}^e} \mathbf{b}_0 N^A \mathrm{d}v$$
$$+ \int_{\mathcal{S}^e} \mathbf{t}_0 N^A \mathrm{d}a + \int_{\mathcal{C}^e} \mathbf{s}_0 N^A \mathrm{d}s \tag{20}$$

and using the corresponding tangents

$$\mathbf{K}_{\mathbf{uu}}^{AB} = -\frac{\partial \mathbf{R}_{\mathbf{u}}^A}{\partial \mathbf{u}^B}. \tag{21}$$

The second term of the right-hand-side of (20) is the non-standard term arising due to the surface tension, requiring the calculation of surface gradients of the shape functions.

The finite-element procedures have been implemented in Abaqus/Standard[33] using a user-element subroutine (UEL). During an analysis, the user subroutine UEL is called for each iteration in a given increment. The initial nodal coordinates as well as the current guesses of the nodal displacements are passed into the subroutine, and the nodal residuals (20) and consistent tangents (21) are required as outputs. We have developed four-noded isoparametric quadrilateral plane-strain and axisymmetric user-elements. We report the details of the calculation of the surface tension contribution to (20) and (21) in both plane strain and axisymmetric settings in Appendix B. In order to avoid issues related to volumetric-locking, we utilize the *F*-bar method of de Souza Neto *et al.*[35] for fully-integrated elements. We have made our Abaqus user-element subroutine available online as ESI.†

4 Numerical simulations

Next, we verify and demonstrate our finite-element capability in a number of settings. First, we qualitatively verify simulation results by examining the wetting behavior of an elastic hemispherical droplet. Next, we perform a quantitative verification by comparing analytical and simulation results for the cavitation of an elastomer during the inflation of a void. Finally, we compare simulations to experiments of the Rayleigh–Plateau instability in thin filaments.

4.1 Qualitative verification: wetting of an elastic droplet

In order to verify that the simulation capability produces intuitively correct results, we consider an elastic hemispherical droplet wetting a rigid substrate, shown schematically in
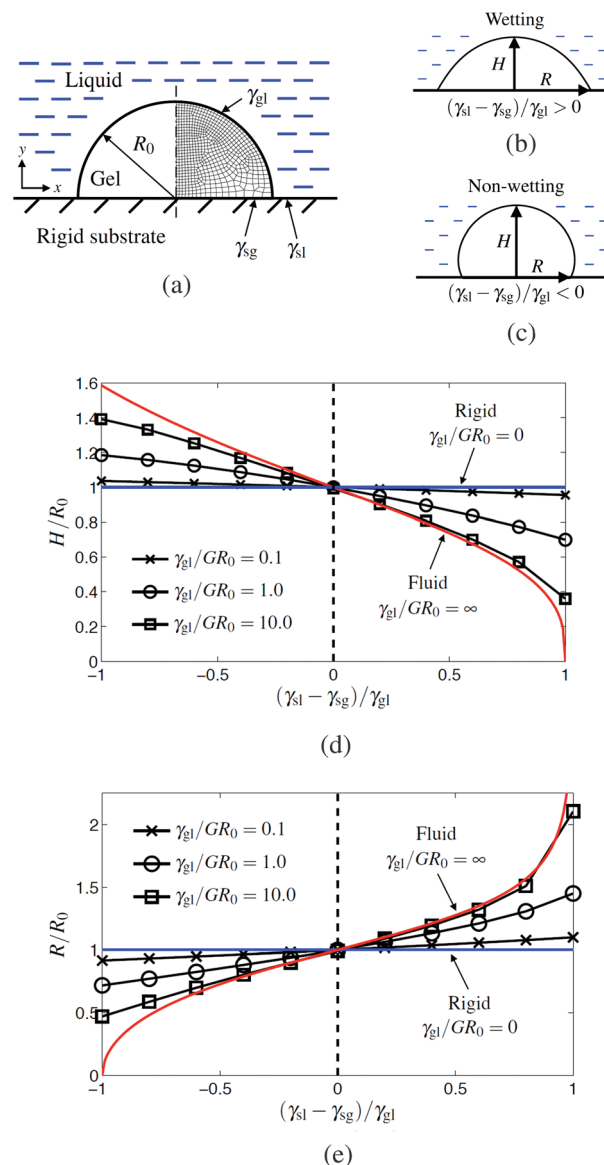

Fig. 2 (a) Initial axisymmetric configuration for a hemispherical elastic droplet on a rigid substrate. Deformed droplet outlines corresponding to (b) $(\gamma_{sl} - \gamma_{sg})/\gamma_{gl} = 0.6$ and $\gamma_{gl}/GR_0 = 1.0$ for the wetting case and (c) $(\gamma_{sl} - \gamma_{sg})/\gamma_{gl} = -0.6$ and $\gamma_{gl}/GR_0 = 1.0$ for the non-wetting case. (d) Height and (e) contact radius of the droplet as a function of $(\gamma_{sl} - \gamma_{sg})/\gamma_{gl}$ for several elasto-capillary numbers.

Fig. 2(a). A fluid droplet would form a constant-curvature spherical cap with a contact angle determined by the surface energies of the three interfaces meeting at the contact line, while a rigid droplet would be unaffected by the surface tension. A soft elastic droplet serves as an intermediate case, undergoing significant deformation dependent upon its initial configuration. We model the initially-hemispherical droplet of radius R_0 in an axisymmetric setting as a Neo-Hookean material using the mesh shown in Fig. 2(a). The nodes along the left side of the mesh form the axis of symmetry with $u_x = 0$, while the nodes along the bottom of the mesh are allowed to move along the rigid surface with $u_y = 0$. The surface tension of the gel–liquid interface is γ_{gl}, the substrate–gel interface γ_{sg}, and the

substrate–liquid interface γ_{sl}. During the course of the simulation, all three surface tensions are ramped linearly from zero. The gel–liquid and substrate–gel surface tensions are incorporated in the simulation as internal surface loads, *i.e.* the second term of the right-hand-side of (20), while the substrate–liquid interface enters as an external line force, *i.e.* the last term of (20).

For $(\gamma_{sl} - \gamma_{sg})/\gamma_{gl} > 0$, shown schematically in Fig. 2(b), the droplet wets the substrate but due to elasticity, does not take on a constant curvature shape. Conversely for $(\gamma_{sl} - \gamma_{sg})/\gamma_{gl} < 0$ (Fig. 2(c)), the droplet non-wets the substrate without maintaining constant curvature. To characterize this behavior, we denote the deformed droplet height and contact radius as H and R, respectively. These quantities are plotted in Fig. 2(d) and (e) for a range of the dimensionless parameters $(\gamma_{sl} - \gamma_{sg})/\gamma_{gl}$ and γ_{gl}/GR_0. Also plotted are the cases of a fluid droplet $\gamma_{gl}/GR_0 = \infty$ (in red) and a rigid hemisphere $\gamma_{gl}/GR_0 = 0$ (in blue). We see that for three intermediate, finite cases of the elasto-capillary number, $\gamma_{gl}/GR_0 = 0.1, 1.0, 10.0$, the droplet wetting behavior lies somewhere between these two limits. However, it is also of note that while the macroscopic deformation of the droplet depends strongly on the elasto-capillary number, the contact angle of the droplet still achieves the fluid value $\cos\theta = (\gamma_{sl} - \gamma_{sg})/\gamma_{gl}$ at the contact line. This is because the force balance sufficiently close to the contact line is dominated by the surface tensions (see (4)), rather than the elastic forces, leading to the same behavior as a fluid. These simulations verify that the simulation capability is able to faithfully describe a complex elasto-capillary setting, involving both non-constant surface tension and contact lines.

4.2 Quantitative verification: cavitation of an elastomer

Next, we quantitatively verify the capability by comparing simulation results against an analytical description of cavitation of a void in an elastomeric Neo-Hookean material. We first consider by a small spherical void of radius R_0 in an infinite elastomeric material, in order to test the axisymmetric code. The initial configuration is shown in Fig. 3(a), where we have overlaid the portion of the mesh near the cavity. The nodes along the left side are taken to be on the axis of symmetry $u_x = 0$, and the nodes on the bottom surface are taken to be a symmetry plane $u_y = 0$. We take a traction-free outer surface at a radius of $50R_0$ to approximate an infinite domain. A surface tension of γ is then applied to the inner cavity surface, causing the cavity to contract. Once the desired elasto-capillary number has been achieved, the volume of the spherical cavity is increased, using displacement control, and the associated cavity pressure is calculated. The analytical pressure/cavity-radius expression for axisymmetric inflation is given by[22]

$$\frac{P}{G} = 2\left[\frac{5}{4} - \left(\frac{R_0}{R}\right) - \frac{1}{4}\left(\frac{R_0}{R}\right)^4\right] + 2\frac{\gamma}{GR_0}\left(\frac{R_0}{R}\right), \qquad (22)$$

where R is the deformed cavity radius. Simulation results are plotted along with (22) for several values of the elasto-capillary number, $\gamma/GR_0 = 0, 2, 5, 10$, in Fig. 3(b). We note that for finite values of the elasto-capillary number the cavity radius at zero pressure is less than R_0. Also, a peak arises in the pressure response, setting the cavitation strength and enabling a
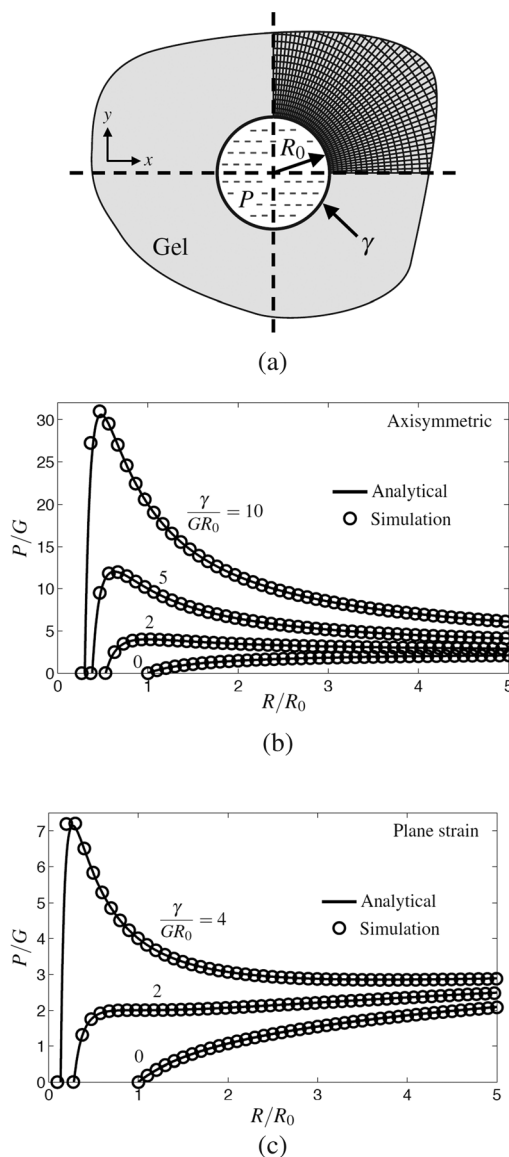

(a)

(b)

(c)

Fig. 3 (a) Initial configuration for cavity inflation in both axisymmetric and plane strain settings. The pressure *versus* radius response for (b) axisymmetric and (c) plane strain cavity inflation comparing analytical and simulation results.

snapping instability.[22] The simulations are able to quantitatively describe all salient features.

Next, we consider a small cylindrical void in an infinite Neo-Hookean material, in order to test the plane strain code. The initial configuration is the same as that shown in Fig. 3(a) but with the left side interpreted as a symmetry plane. The surface tension load and displacement-controlled cavity inflation are applied sequentially as before. The plane strain cavity inflation response is given analytically by

$$\frac{P}{G} = \left[\ln\left(\frac{R}{R_0}\right) + \frac{1}{2}\left(1 - \left(\frac{R_0}{R}\right)^2\right)\right] + \frac{\gamma}{GR_0}\left(\frac{R_0}{R}\right), \qquad (23)$$

where R is the deformed cavity radius. We plot simulation results along with (23) for several values of the elasto-capillary number, $\gamma/GR_0 = 0, 2, 4$, in Fig. 3(c). Again, we note the presence

of surface tension inwardly shifts the zero pressure cavity radius and leads to a peak in the pressure response for sufficiently high surface tension, with these features being quantitatively described by the simulation results.

4.3 Rayleigh–Plateau instability in thin filaments

One of the more interesting elasto-capillary phenomena is the manifestation of the Rayleigh–Plateau instability in an elastic material. In a fluid, this instability causes fluid jets to break up into droplets; however, break-up is prohibited in an elastic material, resulting in a stable undulatory configuration. This phenomena was recently demonstrated experimentally by Mora et al.,[11] using thin ($R_0 = 250$ μm) filaments of agar gel in a toluene solution. In the experiments, the elasto-capillary number was manipulated by varying the shear modulus of the gel by controlling the cross-link density. The experimentally-measured amplitude of the undulatory shape is shown as symbols as a function of elasto-capillary number in Fig. 4(a). It was observed, as well as supported by analytics, that the instability occurs for $\gamma/GR_0 \geq 6$.

The initial finite-element configuration for a filament of radius R_0 is shown in the left inset in Fig. 4(a) with a portion of the axisymmetric mesh overlaid. The left side of the mesh is taken to be the axis of symmetry with $u_x = 0$. We take the filament to have a length of $40R_0$ to approximate an infinitely long filament, and the nodes on top and bottom are prescribed to have $u_y = 0$. Due to large, post-instability deformation, we model the gel as a Gent material. The surface tension is then ramped up on the outer surface. As the elasto-capillary number is increased in this way, we measure the undulatory amplitude of the outer surface, which is plotted as a solid line in Fig. 4(a). The instability initiates at $\gamma/GR_0 \geq 6$, as in the experiment. In order to quantitatively describe the post-instability undulatory amplitude, we take $I_m = 5.37$. Viscoelasticity in the material response is used in this simulation, the details of which are discussed in Appendix A. We reverse the loading by ramping the elasto-capillary number back to zero to ensure that no hysteresis is observed and therefore that the reported results are unaffected by the assumed viscoelastic response.

Next, we examine through simulation the effect of geometry on this instability. Consider an internally-supported tube, shown schematically in the right inset of Fig. 4(b). The nodes along the inner side of this axisymmetric mesh are prescribed to have $u_x = u_y = 0$ and surface tension is applied to the outer side. This case may be thought of as an annular elastomeric layer with outer radius R_0 attached to the outside of a rigid cylinder of radius R_i. For a given radius ratio R_i/R_0, we ramp the elasto-capillary number to the onset of instability. The critical elasto-capillary number at that geometry is then plotted as a point in Fig. 4(b). The $R_i/R_0 = 0$ limit corresponds to a solid filament, for which the critical elasto-capillary number is 6, and the $R_i/R_0 = 1$ limit represents a flat layer, which will not undergo an instability. Fig. 4(b) shows how the onset of this instability transitions smoothly between these two limits.

We consider the converse setting of an externally-supported tube, shown schematically in the right inset of Fig. 4(c). This
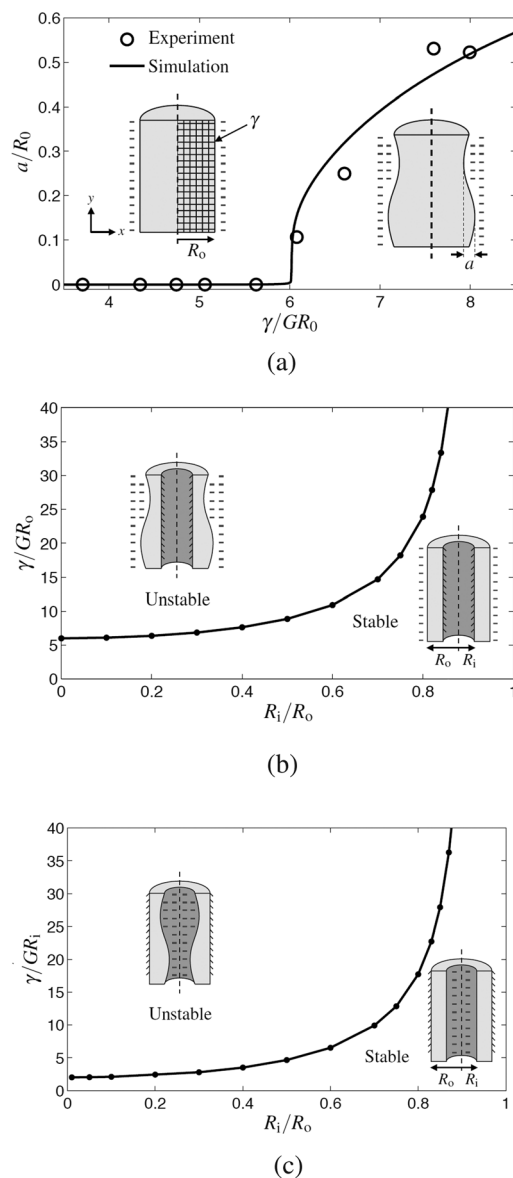

Fig. 4 (a) Undulatory amplitude as a function of elasto-capillary number in both experiments[11] and simulation. Insets: schematics of the undeformed and deformed filaments. Simulated stability maps for (b) internally-supported and (c) externally-supported tubes for a range of elasto-capillary numbers and radius ratios.

case represents an annular elastomeric layer with inner radius R_i attached to the inside of a rigid cylinder of radius R_0. In the simulations, we take $u_x = u_y = 0$ for the nodes along the outer side of the axisymmetric mesh and apply surface tension to the inner side. The stability map is generated in the same way as above and plotted in Fig. 4(c). Again, the $R_i/R_0 = 1$ limit represents a flat layer, which does not undergo an instability. The $R_i/R_0 = 0$ case represents a cylindrical void in an infinite elastomeric matrix. In this case, a Rayleigh–Plateau-like instability occurs for $\gamma/GR_i > 2$, with a smooth transition for intermediate geometries. Instabilities in this geometry have yet to be examined thoroughly, and analytical study of the $R_i/R_0 = 0$ case is needed to corroborate the simulation results.

5 Concluding remarks

In this work, we have presented a simple variational formulation for the elasto-capillary problem and used it as a basis for a robust finite-element formulation. We have implemented four-noded axisymmetric and plane-strain elements in the commercial finite-element program Abaqus/Standard by writing user-element subroutines (UELs). We have qualitatively verified the simulation capability in the case of wetting of an elastic droplet and quantitatively verified the codes by comparing simulation results of cavity inflation against analytics. We have also used the simulation capability to rationalize experiments of the Rayleigh–Plateau instability in soft elastic filaments. The user-element subroutine is available online as ESI.† We expect this work to open the door for further study of elasto-capillary problems.

Appendix

A Viscoelastic material response

In order to directly model elasto-capillary instabilities, it is necessary to include history dependence in our formulation of the problem. Rather than introducing inertia, we incorporate time-dependence into the material response through a simple viscoelastic model. We emphasize that the viscoelastic model is not intended to describe real material behavior; instead it serves as a numerical tool enabling the simulation of instabilities. In this appendix, we briefly summarize this material response, consisting of a finite-deformation Maxwell element in parallel with the hyperelastic behavior of (13) and (14). With reference to the schematic in Fig. 5, branch 1 represents the equilibrium hyperelastic behavior of the material and branch 2 is the Maxwell element introduced to add time dependence.

Mathematically, the viscoelastic constitutive model involves the following fields: $\mathbf{x} = \boldsymbol{\chi}(\mathbf{X}, t)$, motion; $\mathbf{F} = \nabla\boldsymbol{\chi}$, $J = \det\mathbf{F} > 0$, deformation gradient; $\mathbf{F} = \mathbf{F}^{\mathrm{e}}\mathbf{F}^{\mathrm{v}}$, elastic–viscous decomposition of $\mathbf{F}$; $\mathbf{F}^{\mathrm{v}}$, $J^{\mathrm{v}} = \det\mathbf{F}^{\mathrm{v}} = 1$, (isochoric) viscous distortion; $\mathbf{F}^{\mathrm{e}}$, $J^{\mathrm{e}} = \det\mathbf{F}^{\mathrm{e}} > 0$, non-equilibrium elastic distortion; $\mathbf{F}^{\mathrm{e}} = \mathbf{R}^{\mathrm{e}}\mathbf{U}^{\mathrm{e}}$, polar decomposition of $\mathbf{F}^{\mathrm{e}}$; $\mathbf{U}^{\mathrm{e}} = \sum_{\alpha=1}^{3} \lambda_{\alpha}^{\mathrm{e}}\mathbf{r}_{\alpha}^{\mathrm{e}} \otimes \mathbf{r}_{\alpha}^{\mathrm{e}}$, spectral decomposition of $\mathbf{U}^{\mathrm{e}}$; $\mathbf{E}^{\mathrm{e}} = \sum_{\alpha=1}^{3} (\ln \lambda_{\alpha}^{\mathrm{e}})\mathbf{r}_{\alpha}^{\mathrm{e}} \otimes \mathbf{r}_{\alpha}^{\mathrm{e}}$, logarithmic elastic strain; $\mathbf{T}$, $\mathbf{T} = \mathbf{T}^{\top}$, Cauchy stress; $\mathbf{M}^{\mathrm{e}} = J^{\mathrm{e}}\mathbf{R}^{\mathrm{e}\top}\mathbf{T}\mathbf{R}^{\mathrm{e}}$, stress conjugate to elastic

Fig. 5 Rheological analogue of the finite-deformation viscoelastic constitutive model.

strain, $\mathbf{E}^{\mathrm{e}}$; ψ_{R}, free energy density per unit volume of referential space.

The referential free energy density has contributions due to the springs in branches 1 and 2:

$$\psi_{\mathrm{R}} = \psi_{\mathrm{R}}^{(1)} + \psi_{\mathrm{R}}^{(2)}. \tag{24}$$

We take $\psi_{\mathrm{R}}^{(1)}$ to be given by (13) and $\psi_{\mathrm{R}}^{(2)}$ to be given by

$$\psi_{\mathrm{R}}^{(2)} = G_{\mathrm{neq}}|\mathrm{dev}(\mathbf{E}^{\mathrm{e}})|^2, \tag{25}$$

where G_{neq} is the non-equilibrium shear modulus.

The Cauchy stress is given by[36]

$$\mathbf{T} = \mathbf{T}^{(1)} + \mathbf{T}^{(2)}, \tag{26}$$

where $\mathbf{T}^{(1)}$ is given by (14) and

$$\mathbf{T}^{(2)} = J^{\mathrm{e}-1}\mathbf{R}^{\mathrm{e}}\mathbf{M}^{\mathrm{e}}\mathbf{R}^{\mathrm{e}\top} \text{ with } \mathbf{M}^{\mathrm{e}} = \frac{\partial \psi_{\mathrm{R}}^{(2)}}{\partial \mathbf{E}^{\mathrm{e}}} = 2G_{\mathrm{neq}}\mathrm{dev}(\mathbf{E}^{\mathrm{e}}). \tag{27}$$

The evolution of $\mathbf{F}^{\mathrm{v}}$ is given by

$$\dot{\mathbf{F}}^{\mathrm{v}} = \mathbf{D}^{\mathrm{v}}\mathbf{F}^{\mathrm{v}}, \ \mathbf{F}^{\mathrm{v}}(\mathbf{X}, t = 0) = 1, \tag{28}$$

with $\mathbf{D}^{\mathrm{v}}$ given by

$$\mathbf{D}^{\mathrm{v}} = \frac{1}{2\eta}\mathrm{dev}(\mathbf{M}^{\mathrm{e}}), \tag{29}$$

where η is the Maxwell element viscosity. Note that since $\psi_{\mathrm{R}}^{(2)}$ is taken to not depend upon J^{e}, the contribution of branch 2 to the stress is purely deviatoric. In this way, we have only added viscoelasticity to the shear deformation and left the volumetric response of (13) and (14) unaffected. For a recent use of a similar viscoelastic material model in a different setting see Chester.[37] This viscoelastic response is only used in the simulations of Section 4.3. The viscoelastic material parameters $\{G_{\mathrm{neq}}, \eta\}$ are taken in this case to be $G_{\mathrm{neq}} = G/10$ and $\eta = (1 \times 10^{-5} \text{ s})G$. We reiterate that all results reported in this paper depend only upon the equilibrium response of branch 1, and that the presence of branch 2 and the values of the material parameters only serve to facilitate the numerics.

B Finite element details

In this section, we describe the calculation of the surface tension contribution to the residuals (20),

$$(\mathbf{R}_{\mathbf{u}}^{\gamma})^A = -\int_{\mathscr{S}^{\mathrm{e}}} \gamma\,\mathrm{grad}_{\mathscr{S}} N^A \mathrm{d}a, \tag{30}$$

and corresponding consistent tangents (21) for four-noded isoparametric quadrilateral plane-strain and axisymmetric user-elements. We follow the work of Saksono and Perić,[29] drawing on elements of differential geometry.[23,28]

B.1 Plane-strain element

Consider the four-noded, quadrilateral plane-strain element shown schematically in Fig. 6. The element face formed by nodes 1 and 2 coincides with the free surface and is acted upon
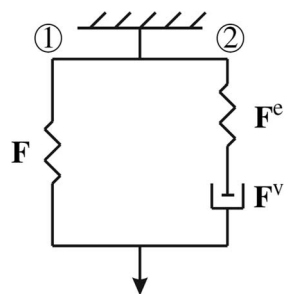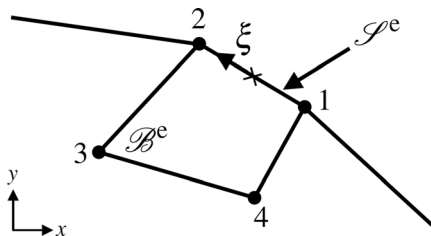
Fig. 6 Schematic of the four-noded quadrilateral plane-strain element.

by surface tension. The shape functions for nodes 1 and 2 are given by

$$N^1 = \frac{1}{2}(1-\xi) \text{ and } N^2 = \frac{1}{2}(1+\xi), \tag{31}$$

respectively, with $-1 \le \xi \le 1$. We write the matrix of shape functions for the face 1–2 as

$$\mathbb{N}(\xi) = \begin{bmatrix} \frac{1}{2}(1-\xi) & 0 & \frac{1}{2}(1+\xi) & 0 \\ 0 & \frac{1}{2}(1-\xi) & 0 & \frac{1}{2}(1+\xi) \end{bmatrix}, \tag{32}$$

so that the position vector for points along the face 1–2 may be parametrized by ξ as

$$\mathbf{x}(\xi) = \mathbb{N}(\xi) \begin{bmatrix} x^1 \\ y^1 \\ x^2 \\ y^2 \end{bmatrix}, \tag{33}$$

where x^A and y^A are the nodal coordinates.

The single relevant metric component in plane strain is

$$A = \frac{d\mathbf{x}(\xi)}{d\xi} \cdot \frac{d\mathbf{x}(\xi)}{d\xi} = \frac{L_e^2}{4}, \tag{34}$$

where $L_e = \sqrt{(x^1-x^2)^2 + (y^1-y^2)^2}$ is the length of the face 1–2. The surface gradient of a scalar field is then given by

$$\text{grad}_{\mathscr{S}}(\cdot) = \frac{1}{A} \frac{d\mathbf{x}(\xi)}{d\xi} \frac{d(\cdot)}{d\xi}, \tag{35}$$

where $A^{-1} d\mathbf{x}(\xi)/d\xi$ is the in-plane contravariant basis vector. Finally, the incremental area is given by

$$da = h\sqrt{A} d\xi, \tag{36}$$

where h is the out-of-plane thickness, typically taken to be unity.

The vector of the surface tension contribution to the element-level residuals (30),

$$\mathbb{R}^\gamma = \left[\left(R_{u_x}^\gamma\right)^1 \left(R_{u_y}^\gamma\right)^1 \left(R_{u_x}^\gamma\right)^2 \left(R_{u_y}^\gamma\right)^2 \right]^\top, \tag{37}$$

is then given by

$$\mathbb{R}^\gamma = -\int_{-1}^{1} \gamma h \frac{1}{\sqrt{A}} \left[\frac{d\mathbb{N}}{d\xi}\right]^\top \frac{d\mathbf{x}(\xi)}{d\xi} d\xi, \tag{38}$$

which, when the surface tension is constant, may be directly calculated as

$$\mathbb{R}^\gamma = -\frac{\gamma h}{L_e} \begin{bmatrix} x^1 - x^2 \\ y^1 - y^2 \\ x^2 - x^1 \\ y^2 - y^1 \end{bmatrix}. \tag{39}$$

Taking the derivative of (39) with respect to the nodal coordinates (and recalling the negative sign in (21)) yields the corresponding contribution to the tangents

$$\mathbb{K}^\gamma = \frac{\gamma h}{L_e} \begin{bmatrix} 1 & 0 & -1 & 0 \\ 0 & 1 & 0 & -1 \\ -1 & 0 & 1 & 0 \\ 0 & -1 & 0 & 1 \end{bmatrix} - \frac{\gamma h}{L_e^3} \begin{bmatrix} x^1 - x^2 \\ y^1 - y^2 \\ x^2 - x^1 \\ y^2 - y^1 \end{bmatrix} \begin{bmatrix} x^1 - x^2 \\ y^1 - y^2 \\ x^2 - x^1 \\ y^2 - y^1 \end{bmatrix}^\top. \tag{40}$$

B.2 Axisymmetric element

The four-noded, quadrilateral axisymmetric element is slightly more complex due to the out-of-plane curvature. The process for deriving residuals and tangents is analogous to that followed in the previous section, and the details may be found in Saksono and Perić.[29] Here, for brevity, we simply report the final result, employing our sign conventions. With nodal coordinates r^A and z^A, the vector of the surface tension contribution to the residuals for face 1–2 of an axisymmetric element is

$$\mathbb{R}^\gamma = -\frac{\pi\gamma(r^1+r^2)}{L_e} \begin{bmatrix} r^1 - r^2 \\ z^1 - z^2 \\ r^2 - r^1 \\ z^2 - z^1 \end{bmatrix} - \pi\gamma L_e \begin{bmatrix} 1 \\ 0 \\ 1 \\ 0 \end{bmatrix}, \tag{41}$$

and the consistent tangent contribution is

$$\mathbb{K}^\gamma = \frac{\pi\gamma}{L_e} \begin{bmatrix} 2r^1 & 0 & -2r^2 & 0 \\ (z^1-z^2) & (r^1+r^2) & (z^1-z^2) & -(r^1+r^2) \\ -2r^1 & 0 & 2r^2 & 0 \\ -(z^1-z^2) & -(r^1+r^2) & -(z^1-z^2) & (r^1+r^2) \end{bmatrix}$$

$$- \frac{\pi\gamma(r^1+r^2)}{L_e^3} \begin{bmatrix} r^1-r^2 \\ z^1-z^2 \\ r^2-r^1 \\ z^2-z^1 \end{bmatrix} \begin{bmatrix} r^1-r^2 \\ z^1-z^2 \\ r^2-r^1 \\ z^2-z^1 \end{bmatrix}^\top + \frac{\pi\gamma}{L_e} \begin{bmatrix} 1 \\ 0 \\ 1 \\ 0 \end{bmatrix} \begin{bmatrix} r^1-r^2 \\ z^1-z^2 \\ r^2-r^1 \\ z^2-z^1 \end{bmatrix}^\top. \tag{42}$$

References

1 P.-G. de Gennes, F. Brochard-Wyart and D. Quéré, *Capillarity and Wetting Phenomena: Drops, Bubbles, Pearls, Waves*, Springer, New York, 1st edn, 2003.

2 B. Roman and J. Bico, *J. Phys.: Condens. Matter*, 2010, **22**, 493101.

3 M. P. Stoykovich, H. B. Cao, K. Yoshimoto, L. E. Ocola and P. F. Nealey, *Adv. Mater.*, 2003, **15**, 1180–1184.

4 A. Jagota, D. Paretkar and A. Ghatak, *Phys. Rev. E: Stat., Nonlinear, Soft Matter Phys.*, 2012, **85**, 051602.

5 A. Carré, J.-C. Gastel and M. E. R. Shanahan, *Nature*, 1996, **379**, 432–434.

6 E. R. Jerison, Y. Xu, L. A. Wilen and E. R. Dufresne, *Phys. Rev. Lett.*, 2011, **106**, 186103.

7 R. W. Style and E. R. Dufresne, *Soft Matter*, 2012, **8**, 7177–7184.

8 R. W. Style, R. Boltyanskiy, Y. Che, J. S. Wettlaufer, L. A. Wilen and E. R. Dufresne, *Phys. Rev. Lett.*, 2013, **110**, 066103.

9 A. Marchand, S. Das, J. H. Snoeijer and B. Andreotti, *Phys. Rev. Lett.*, 2012, **108**, 094301.

10 A. Marchand, S. Das, J. H. Snoeijer and B. Andreotti, *Phys. Rev. Lett.*, 2012, **109**, 236101.

11 S. Mora, T. Phou, J.-M. Fromental, L. M. Pismen and Y. Pomeau, *Phys. Rev. Lett.*, 2010, **105**, 214301.

12 E. Hohlfeld and L. Mahadevan, *Phys. Rev. Lett.*, 2011, **106**, 105702.

13 J. Yoon, J. Kim and R. C. Hayward, *Soft Matter*, 2010, **6**, 5807–5816.

14 D. Chen, S. Cai, Z. Suo and R. C. Hayward, *Phys. Rev. Lett.*, 2012, **109**, 038001.

15 S. Mora, M. Abkarian, H. Tabuteau and Y. Pomeau, *Soft Matter*, 2011, **7**, 10612–10619.

16 J. A. Zimberlin, N. Sanabria-DeLong, G. N. Tew and A. J. Crosby, *Soft Matter*, 2007, **3**, 763–767.

17 S. Kundu and A. J. Crosby, *Soft Matter*, 2009, **5**, 3963–3968.

18 J. A. Zimberlin, J. J. McManus and A. J. Crosby, *Soft Matter*, 2010, **6**, 3632–3635.

19 A. J. Crosby and J. J. McManus, *Phys. Today*, 2011, **64**, 62–63.

20 J. Cui, C. H. Lee, A. Delbos, J. J. McManus and A. J. Crosby, *Soft Matter*, 2011, **7**, 7827–7831.

21 A. Delbos, J. Cui, S. Fakhouri and A. J. Crosby, *Soft Matter*, 2012, **8**, 8204–8208.

22 J. Zhu, T. Li, S. Cai and Z. Suo, *J. Adhes.*, 2011, **87**, 466–481.

23 M. E. Gurtin and A. I. Murdoch, *Arch. Ration. Mech. Anal.*, 1975, **57**, 291–323.

24 P. H. Leo and R. F. Sekerka, *Acta Metall.*, 1989, **37**, 3119–3138.

25 M. E. Gurtin and A. Struthers, *Arch. Ration. Mech. Anal.*, 1990, **112**, 97–160.

26 N. K. Simha and K. Bhattacharya, *J. Mech. Phys. Solids*, 1998, **46**, 2323–2359.

27 N. K. Simha and K. Bhattacharya, *J. Mech. Phys. Solids*, 2000, **48**, 2619–2641.

28 P. Steinmann, *J. Mech. Phys. Solids*, 2008, **56**, 772–800.

29 P. H. Saksono and D. Perić, *Comput. Mech.*, 2006, **38**, 265–281.

30 A. Javili and P. Steinmann, *Comput. Meth. Appl. Mech. Eng.*, 2009, **198**, 2198–2208.

31 A. Javili and P. Steinmann, *Comput. Meth. Appl. Mech. Eng.*, 2010, **199**, 755–765.

32 A. Papastavrou, P. Steinmann and E. Kuhl, *J. Mech. Phys. Solids*, 2013, **61**, 1446–1463.

33 Abaqus, Reference Manuals, 2010.

34 A. N. Gent, *Rubber Chem. Technol.*, 1996, **69**, 59–61.

35 E. A. de Souza Neto, D. Perić, M. Dutko and D. R. J. Owen, *Int. J. Solids Struct.*, 1996, **33**, 3277–3296.

36 L. Anand, N. M. Ames, V. Srivastava and S. A. Chester, *Int. J. Plast.*, 2009, **25**, 1474–1494.

37 S. A. Chester, *Soft Matter*, 2012, **8**, 8223–8233.